Resolving the Overlap of Macrovascular and Microvascular Flow Components in Digital Subtraction Angiography for Cerebral Reperfusion Assessment

Chengchuan Wu[1][0000-0002-9642-8970], Catherine Davey[2][0000-0002-5672-7941],
Gagan Sharma[3], and Felix Ng[1,4][0000-0001-6973-8677]

[1] Department of Medicine, The University of Melbourne, Australia
`chengchuan.wu@unimelb.edu.au`
[2] Department of Biomedical Engineering, The University of Melbourne, Australia
[3] Melbourne Brain Centre, Australia
[4] The Royal Melbourne Hospital, Australia

Abstract. Cerebral digital subtraction angiography (DSA) is an Xray-based imaging modality that provides high-resolution, real-time visualisation of cerebral vasculature, and is an established part of the standard treatment of stroke patients. Conventionally, DSA data are acquired as 2D images where vessel structures overlap with one another due to the penetrating nature of X-ray. Given the increasing recognition of the importance of microvasculatures in stroke, there is an unmet need to utilise DSA to accurately assess microvessels, unobstructed from overlapping macrovessels. This work proposes a novel Expectation-Maximisation algorithm integrated with anatomy-informed regularisation to disentangle macrovascular and microvascular flow component overlaps in a spatiotemporal Gamma mixture model for DSA. In-vivo experiments across 108 stroke patients demonstrate that the proposed method achieves robust estimation and provides clear separation of the macrovascular and microvascular flow components. Based on the proposed method, quantitative microvascular cerebral blood volume was derived from DSA images and shown to be significantly associated with the current gold-standard reperfusion metric.

Keywords: Digital subtraction angiography (DSA) · Perfusion · Ischemic stroke · Mixture model.

1 Introduction

Cerebral digital subtraction angiography (DSA) is an Xray-based, time-resolved imaging technique to visualise vessels with high spatiotemporal resolution in real-time [1]. DSA forms the foundation of modern endovascular treatments and diagnosis of many neurovascular diseases such as ischemic stroke, aneurysm and vascular malformation, providing real-time visualisation of the vasculature tree to enable catheter navigation and lesion localisation [1].

A primary example of the importance of DSA in clinical practice is the DSA-guided endovascular thrombectomy (EVT), a first-line treatment for acute ischemic stroke caused by large vessel occlusions [2, 3]. In EVT, catheters are carefully navigated, starting from the lower limb, to mechanically extract a clot from the brain under real-time visualisation of DSA. A final biplane DSA acquisition of the affected arterial territory is routinely performed at the end of the EVT to assess the extent of reperfusion as a key measure of procedural success [4]. This final acquisition also aids in early prognostication and provides a mean to screen for potential intraprocedural complications that may require further immediate treatment [1]. Despite its usefulness, DSA-based reperfusion assessments have multiple key limitations. Firstly, the current gold standard metric of reperfusion, Thrombolysis in Cerebral Infarction (TICI) score (Table 1), is observational and qualitative, and thus subject to inter-rater variability [5], limiting its prediction of functional outcomes [4]. Deep learning-based models to score TICI have been developed to address the subjectiveness but have not seen a significantly improved prediction of functional outcomes [6, 7]. Secondly, recent studies [8–10] have shown that brain tissue may remain occluded at the microscopic level despite apparent normalised macrovascular flow on visual assessment of DSA. Hence, direct assessment of microvascular perfusion in parenchyma, the ultimate goal of treatment in ischemic stroke, is required to avoid underdetecting such important and potentially treatable pathologies.

Table 1. Definition of extended TICI (eTICI) [4], a widely used variant of the TICI scoring system.

eTICI	**Definition**
0	No reperfusion or antegrade flow is observed beyond the occlusion site.
1	Blood flows penetrate the occlusion but only minimal tissue reperfusion.
2A	Less than 50% reperfusion in the downstream territory.
2B	More than 50% reperfusion in the downstream territory.
2C	Near complete reperfusion, but delayed flows or small emboli are observed in the distal downstream territory.
3	Complete reperfusion.

Deconvolution-based DSA perfusion (DSAP) [11] is a promising method for assessing post-EVT reperfusion, which processes source DSA data to derive quantitative perfusion parameters, such as cerebral blood volume (CBV), cerebral blood flow (CBF) and mean transit time (MTT). In the first published attempt to derive DSAP on 66 acute ischemic stroke patients, CBV and CBF were shown to be weakly associated with TICI scores without reaching statistical significance [11]. In another proof-of-concept study involving 50 stroke cohorts, MTT was shown to be associated with post-EVT hemorrhagic transformation [12]. The robustness of the deconvolution-based DSAP against contrast injection protocols and sensitivity to cerebral hemodynamics were further validated on swine models [13]. Given these initial results that demonstrate the feasibility of DSAP, there is obvious interest in further clinical validation.

One of the challenges in objectively measuring the TICI score and deriving DSAP is the anatomical overlap of multiple vascular components in 2D DSA images. For example, subtle abnormalities of the microvessels, such as no-reflow [8, 10], may be obscured by overlying and surrounding macrovessels. Prior attempt [11] to mitigate this problem by a mixture model was only able to exclude veins, while arteries remained and continued to confound the microvascular reperfusion assessment. Given that microvascular reperfusion is of high clinical importance [8, 10, 14], a solution to extract the microvascular component from DSA is in clear need.

In this work, we describe a novel method that enables robust and accurate separation of the macrovascular and microvascular flow components for DSA. Furthermore, we used the resultant microvascular components to produce microvascular DSAP images on 108 stroke patients and demonstrated their association with core lab-assessed TICI, the current gold standard in clinical practice.

2 Theoretical Background

2.1 Pixel-wise Gamma-variate Mixture Model

A pixel-wise gamma-variate mixture model (P-GMM) and the corresponding Expectation-Maximisation (EM) algorithm (P-EM) were proposed to resolve overlapping DSA concentration curves [11]. In this work, we implemented P-GMM and P-EM as a benchmark, described below.

P-GMM assumes that contrast agent particles injected into the blood arrive at a downstream anatomical location with arrival times that follow a gamma distribution with shape, α, and scale, β, assumed to be determined by the local flow condition. Due to the projected nature of DSA, particles appear in the same pixel can be originated from various overlapped anatomical components, such as arteries, capillaries or veins. In a pixel, the event that a particle originated from a component, Z, appears at time, T, follows a gamma mixture distribution, with complete probability,

$$P\left(T=t, Z=k|\mathbf{\Theta}\right)=\prod_{k=1}^{K}\left(\tau_k\gamma\left(t|\alpha_k,\beta_k\right)\right)^{I(Z=k)}, \tag{1}$$

where I is the binary indicator, mixture parameter set $\mathbf{\Theta}=\{\alpha_k,\beta_k,\tau_k\}$, τ_k is the proportion of the k-th component and K denotes the total number of components.

Resolution of the mixture at the pixel can be achieved by the estimation of $\mathbf{\Theta}$, which can be sought at the maximum of the complete log-likelihood

$$\mathcal{L}\left(\mathbf{\Theta}|T,Z\right)=\sum_{i=1}^{N}\sum_{l=1}^{C(t_i)}\sum_{k=1}^{K}I\left(Z_l=k\right)\log\left(\tau_k\gamma\left(t_i|\alpha_k,\beta_k\right)\right), \tag{2}$$

where subscriptions i, k, l denote the indices of time points, gamma components and particles, respectively, N denotes the total number of temporal sampling points and $C(t)$ denotes contrast concentration, which corresponds to the repetition of particle events at t and can be approximated by the inversed pixel intensity (maximum intensity minus raw pixel intensity).

2.2 Pixel-wise Expectation-Maximisation Algorithm

Given observed data, $C(t)$, measured at a pixel, and the marginal log-likelihood $\mathcal{L}_T\left(\mathbf{\Theta}|T\right)$, measured at time, T, the P-EM algorithm iteratively finds a local log-likelihood maxima, following the E-step and the M-step.

E-step: Define $Q\left(\mathbf{\Theta}|\mathbf{\Theta}^{(m)}\right)$ as the expected value of the log-likelihood of $\mathbf{\Theta}$, with respect to the conditional distribution of Z, given T and $\mathbf{\Theta}^{(m)}$ at the m-th step:

$$Q\left(\mathbf{\Theta}|\mathbf{\Theta}^{(m)}\right) = \sum_{i=1}^{N}\sum_{k=1}^{K} C(t_i) z_{ik}^{(m)} \log\left(\tau_k \gamma\left(t_i|\alpha_k, \beta_k\right)\right), \tag{3}$$

where $z_{ik}^{(m)}$ is the conditional expectation of $I\left(Z_l = k\right)$, which indicates the l-th particle at t_i coming from the k-th component, estimated given $\mathbf{\Theta}^{(m)}$:

$$z_{ik}^{(m)} = P\left(Z_l = k|t_i\right) = \frac{\tau_k^{(m)}\gamma\left(t_i|\alpha_k^{(m)}, \beta_k^{(m)}\right)}{\sum_{\kappa=1}^{K}\tau_\kappa^{(m)}\gamma\left(t_i|\alpha_\kappa^{(m)}, \beta_\kappa^{(m)}\right)}. \tag{4}$$

M-step: Find $\mathbf{\Theta}^{(m+1)}$ to maximise the expected value of the log-likelihood

$$\mathbf{\Theta}^{(m+1)} = \arg\max_{\mathbf{\Theta}} Q\left(\mathbf{\Theta}, \mathbf{\Theta}^{(m)}\right), \tag{5}$$

where $\mathbf{\Theta} = \{\alpha_k, \beta_k, \tau_k; k = 1, \ldots, K\}$.

2.3 DSA Intensity Reconstruction

Reconstructed DSA intensity of the k-th component in a pixel is given by:

$$\hat{C}_k\left(t_i\right) = S\,\hat{\tau}_k\gamma\left(t_i|\hat{\alpha}_k, \hat{\beta}_k\right), \tag{6}$$

where $S = \sum_{i=1}^{N} C(t_i)$ is the scaling factor and $\hat{\cdot}$ denotes estimation.

3 Theory

3.1 Neighbourhood-wise Gamma Mixture Model

To improve the estimation of $\mathbf{\Theta}$, this work proposes neighbourhood-wise gamma mixture model (N-GMM), a modification of P-GMM, that expands the formalism from individual pixels to their neighbourhoods (Figure 1).

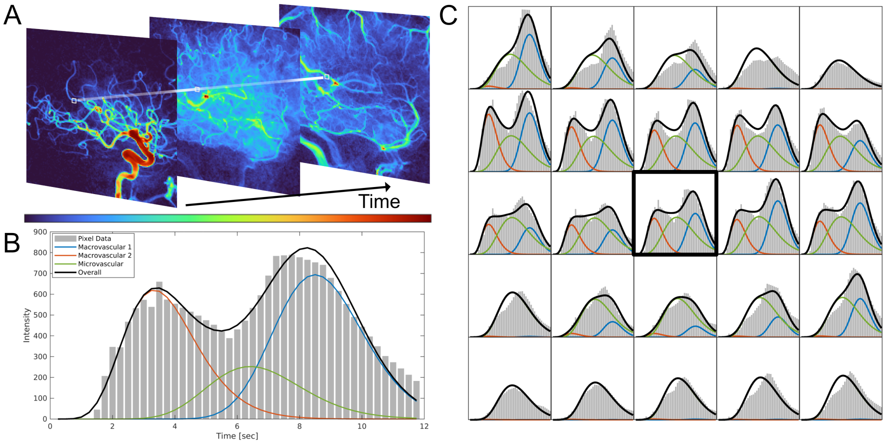

Fig. 1. Illustration of P-EM and N-EM. (A) Frames selected from a lateral DSA run. The white box indicates a 5 × 5 neighbourhood. (B) P-EM fits the P-GMM to the central pixel, using only the data of that pixel. (C) In contrast, N-EM fits the N-GMM of the neighbourhood to solve for the parameters of the central pixel. Panels display the intensities at corresponding locations in the box. Gray bars represent pixel intensity data and curves represent the reconstructed intensities.

Based on the observation that vascular flow patterns are highly similar in an anatomical vicinity, N-GMM assumes that gamma parameters α_k, β_k of the k-th components are identical in a pre-defined neighbourhood. Where pixels are indexed by $p \in \{1, ..., P\}$, the spatially varying contribution is defined by weights, τ_{pk}, across the pixel neighbourhood. Thus, for the parameter set of a neighbourhood, $\mathbf{\Theta} = \{\alpha_k, \beta_k, \tau_{pk}\}$, the log-likelihood becomes

$$\mathcal{L}^* \left(\mathbf{\Theta}|T, Z\right) = \log \prod_{p=1}^{P} \prod_{i=1}^{N} \prod_{l=1}^{C_p(t_i)} \prod_{k=1}^{K} \left(\tau_{pk} \gamma \left(t_i|\alpha_k, \beta_k\right)\right)^{I(Z_{pl}=k)} . \tag{7}$$

3.2 Neighbourhood-wise Expectation-Maximisation Algorithm

The N-GMM allows a designated EM algorithm-based estimator, N-EM, to incorporate prior knowledge from the neighbourhood. Based on Equation 7, an EM algorithm solution was proposed, with modifications to the optimisation as shown below.

Vessel Segmentation: a segmentation mask was provided to the optimisation to identify “tissue pixels”, P_t, which do not contain any apparent vessel structure in the DSA. Frangi filtering [15] was applied to each frame to obtain a set of scores for each pixel. A pixel is then classified into P_t if its maximum score is below a threshold, F_{th}.

Constraints to Tissue Pixels: To employ the constraint that GMM will degrade to a single gamma model in tissue pixels, a sufficiently low, empirical upper limit, $U = 0.01$, is applied to the proportion weight of all macrovascular components, K_M, in those pixel. That is, $\tau_{pk} < U$ for $p \in P_t$ and $k \in K_M$.

Regularisation with Respect to the Microvascular Component: To account for the observation that microvascular perfusion varies smoothly in the brain, a regularisation term, which represents the intra-neighbourhood variance of the microvascular component intensities, is introduced to the optimisation:

$$R = \frac{-\lambda}{P-1} \sum_{p} \left(\sum_{i} C_p\left(t_i\right) \tau_{pk_m} - \frac{1}{P} \sum_{i,\rho} C_\rho\left(t_i\right) \tau_{\rho k_m} \right)^2 , \tag{8}$$

where λ is the regularisation parameter and k_m is the microvascular component.

Spatial Gaussian Weighting: A Gaussian weighting kernel $w\left(x,y\right) = \exp\left\{-\left(x^2+y^2\right)/\left(2\sigma^2\right)\right\}/\left(2\pi\sigma^2\right)$ is applied to the neighbourhood in the objective function, where x, y are the 2D distances with respect to the central pixel and σ^2 is the variance.

Optimisation: Incoporating the above modification, the complete objective function for the N-EM algorithm becomes

$$\begin{aligned} Q\left(\boldsymbol{\Theta}|\boldsymbol{\Theta}^{(m)}\right) &= \sum_{p=1}^{P}\sum_{i=1}^{N}\sum_{k=1}^{K} w_p C_p(t_i) z_{pik}^{(m)} \log\left(\tau_{pk}\gamma\left(t_i|\alpha_k,\beta_k\right)\right) + R, \\ z_{pik}^{(m)} &= \frac{\tau_{pk}^{(m)}\gamma\left(t_i|\alpha_k^{(m)},\beta_k^{(m)}\right)}{\sum_{\kappa=1}^{K}\tau_{p\kappa}^{(m)}\gamma\left(t_i|\alpha_\kappa^{(m)},\beta_\kappa^{(m)}\right)}. \end{aligned} \tag{9}$$

The optimisation formula is

$$\begin{aligned} &\boldsymbol{\Theta}^{(m+1)} = \arg\max_{\boldsymbol{\Theta}} Q\left(\boldsymbol{\Theta},\boldsymbol{\Theta}^{(m)}\right), \\ s.t. \quad &\sum_k \tau_{pk} = 1, \quad \forall p; \quad 0 < \tau_{pk} < U, \quad p \in P_t, k \in K_M; \\ &0 < \tau_{pk} < 1, \quad \forall p,k; \quad 0 < \alpha_k, \quad \forall k; \qquad 0 < \beta_k, \quad \forall k, \end{aligned} \tag{10}$$

where $\boldsymbol{\Theta} = \{\alpha_k, \beta_k, \tau_{pk}; k = 1, \ldots, K, p = 1, \ldots, P\}$.

4 Methods

4.1 Implementations

We empirically defined the neighbourhood as a square region of 81 pixels for N-GMM, and set $\sigma = 4$, $\lambda = 10^{-3}$, and $K = 3$, allowing for the presence of arterial (macrovascular), venous (macrovascular) and parenchymal (microvascular) flows. For vessel masking, Frangi's $\beta = 0.8$, $c = 100$, $\sigma = \{1, 2\}, F_{th} = 0.1$. N-EM optimisation was initialised by K-means and solved using the interior-point method in MATLAB (2024b). The EM iteration terminated when $|Q^{(m+1)} - Q^{(m)}| < 5 \times 10^{-4}$ or after 30 iterations. As a referenced method, P-GMM was implemented with parameters matching the N-GMM counterpart where applicable.

4.2 Experiments

We tested N-EM on post-EVT bi-plane DSA from 108 patients diagnosed with internal carotid artery or M1 occlusion (eTICI 2A: n=7; 2B: n=51; 2C: n=26; 3: n=24) in EXTEND-IA TNK Part 1 & 2 clinical trials. DSA runs with a varying acquisition rate were upsampled to the highest rate (median = 4 fps) using linear interpolation. All image sizes were resampled to 224×224. We used the coefficient of determination, R^2, to measure the goodness of fit in each pixel, given as

$$R^2 = 1 - \frac{\sum_i (C(t_i) - \hat{C}(t_i))^2}{\sum_i (C(t_i) - \sum_j C(t_j)/N)^2}. \tag{11}$$

To validate the potential clinical applicability of N-EM, we derived the CBV corresponding to the separated microvascular component based on deconvolution [11], where the arterial input function was measured from the internal carotid artery in the macrovascular component image. The mean CBV value (mCBV) was calculated over the middle cerebral artery (MCA) territory. Frontal mCBV and lateral mCBV were each fitted to extended TICI (eTICI) using ordinal regression, where the association was assessed by Wald test.

5 Results

Both P-EM and N-EM achieved good fits to the data, as indicated by high R^2 values (P-EM: $R^2 = 0.87 \pm 0.07$, N-EM: $R^2 = 0.81 \pm 0.09$). However, artifacts in regions with vessel overlaps are observed in the microvascular images produced by P-EM (Figure 2C), whereas they do not appear in the images derived from N-EM (Figure 2E).

CBV computed from the deconvolution of the N-EM microvascular image contains minimal vascular contribution (Figure 3A). Ordinal regressions show that core-lab eTICI scores are significantly associated with both frontal mCBV ($p<0.001$, Figure 3B) and lateral mCBV ($p=0.015$, Figure 3C).

6 Discussion and Conclusion

N-EM achieves visually improved separation. Artifacts in P-EM (Figure 2C) might have originated from two causes. Firstly, the gamma probability density function is intrinsically flexible. As a consequence, while P-EM can successfully separate arterial and venous overlaps with $K = 2$ in P-GMM [11], it might become susceptible to overfitting when K increases to 3 to include the additional parenchymal component. Secondly, solving P-GMM with substantial overlaps as an inverse problem might be ill-conditioned, prohibiting reliable solutions under the influence of noise. In contrast, N-EM presents smooth microvascular images (Figure 2E). N-EM extends the framework from a pure temporal domain to a spatiotemporal domain to gather more data for the mixture model. While DSA intensities collected from adjacent pixels might exhibit various shapes, the

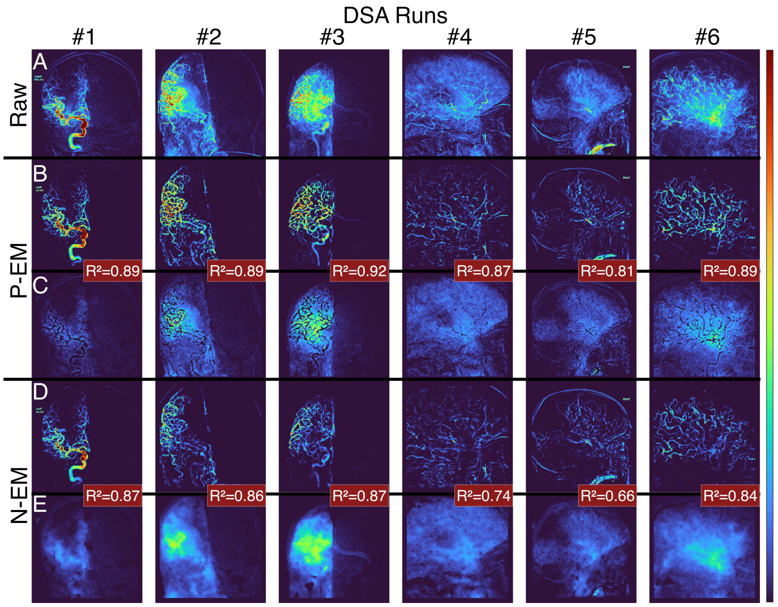

Fig. 2. (A) Raw images from six DSA examples. (B) Reconstructed macrovascular images, each was the superposition of two corresponding macrovascular gamma components, and (C) recontructed microvascular images obtained from P-EM. (D) Reconstructed macrovascular images and (E) microvascular images from N-EM. We calculated R^2 according to Equation 11 and averaged the values over the MCA territory.

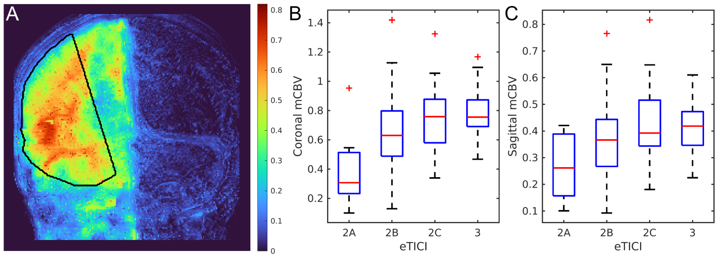

Fig. 3. (A) Representative microvascular CBV image (unitless). The black outline indicates the MCA territory. Box plots showing (B) frontal mCBV and (C) lateral mCBV in eTICI groups. The eTICI score is significantly associated with coronal mCBV ($p<0.001$) and sagittal mCBV ($p=0.015$).

underlying gamma distributions may share very similar parameters. Such increased data heterogeneity could mitigate overfitting. Moreover, vessels in DSA as a distinctive image feature can be recognised by well-developed computer vision techniques, such as Frangi filtering. N-EM encapsulates measurements in vessel-free pixels as unobstructed observations of local microvascular flows to provide prior information for neighbouring pixels, enabling resolution of GMM, even in the presence of substantial overlaps.

The association between mCBV and eTICI suggests that DSA perfusion may also provide supplementary prognostic information for EVT. MCBV is a quantitative measurement exclusive to microvascular perfusion, and therefore could be able to overcome inter-rater variability and vessel-centric evaluation, which are the major drawbacks of TICI. To further improve microvascular perfusion mapping, future studies can focus on temporal perfusion parameters to identify delayed reperfusion and use image-based analysis to assess local lesion signs.

In this work we have presented N-EM, a method that successfully resolves macrovascular and microvascular flow overlaps in DSA. For the first time, we employed the separated components resulted from N-EM to generate DSA microvascular CBV maps, demonstrating its association with core-lab eTICI scores, showing the potential of N-EM in quantitative evaluation of post-EVT outcome for stroke patients.

Disclosure of Interests. The authors have no competing interests to declare that are relevant to the content of this article.

References

1. Shaban, S., Huasen, B., Haridas, A., Killingsworth, M., Worthington, J., Jabbour, P. and Bhaskar, S.M.M.: Digital subtraction angiography in cerebrovascular disease: current practice and perspectives on diagnosis, acute treatment and prognosis. Acta Neurologica Belgica, **122**, 1-18 (2022)
2. Hui, W., Wu, C., Zhao, W., Sun, H., Hao, J., Liang, H., Wang, X., Li, M., Jadhav, A.P., Han, Y. and Ji, X.: Efficacy and safety of recanalization therapy for acute ischemic stroke with large vessel occlusion: a systematic review. Stroke, **51**(7), 2026-2035 (2020)
3. Nguyen, T.N., Abdalkader, M., Fischer, U., Qiu, Z., Nagel, S., Chen, H.S., Miao, Z. and Khatri, P.: Endovascular management of acute stroke. The Lancet, **404**(10459), 1265-1278 (2024)
4. Almekhlafi, M.A., Mishra, S., Desai, J.A., Nambiar, V., Volny, O., Goel, A., Eesa, M., Demchuk, A.M., Menon, B.K. and Goyal, M.: Not all "successful" angiographic reperfusion patients are an equal validation of a modified TICI scoring system. Interventional Neuroradiology, **20**(1), 21-27 (2014)
5. Heiferman, D.M., Pecoraro, N.C., Wozniak, A.W., Ebersole, K.C., Jimenez, L.M., Reynolds, M.R., Ringer, A.J. and Serrone, J.C.: Reliability of the modified TICI score among endovascular neurosurgeons. American Journal of Neuroradiology, **41**(8), 1441-1446 (2020)
6. Su, R., Cornelissen, S.A., Van der Sluijs, M., Van Es, A.C., Van Zwam, W.H., Dippel, D.W., Lycklama, G., van Doormaal, P.J., Niessen, W.J., van der Lugt,

A. and van Walsum, T.: autoTICI: automatic brain tissue reperfusion scoring on 2D DSA images of acute ischemic stroke patients. IEEE transactions on medical imaging, **40**(9), 2380-2391 (2021)

7. Nielsen, M., Waldmann, M., Sentker, T., Frölich, A., Fiehler, J. and Werner, R.: Time matters: handling spatio-temporal perfusion information for automated TICI scoring. In Medical Image Computing and Computer Assisted Intervention 2020, Proceedings Part VI 23, 86-96. Springer (2020).
8. Jia, M., Jin, F., Li, S., Ren, C., Ruchi, M., Ding, Y., Zhao, W. and Ji, X.: No-reflow after stroke reperfusion therapy: An emerging phenomenon to be explored. CNS neuroscience and therapeutics, **30**(2), e14631 (2024)
9. Schönfeld, M.H., Kabiri, R., Kniep, H.C., Meyer, L., Sedlacik, J., Ernst, M., Broocks, G., Faizy, T.D., Cheng, B., Thomalla, G. and Fiehler, J.: Sub-angiographic peripheral emboli in high resolution DWI after endovascular recanalization. Journal of neurology, **267**, 1401-1406 (2020)
10. Ng, F.C., Churilov, L., Yassi, N., Kleinig, T.J., Thijs, V., Wu, T., Shah, D., Dewey, H., Sharma, G., Desmond, P. and Yan, B.: Prevalence and significance of impaired microvascular tissue reperfusion despite macrovascular angiographic reperfusion (no-reflow). Neurology, **98**(8), e790-e801 (2022)
11. Scalzo, F. and Liebeskind, D.S.: Perfusion angiography in acute ischemic stroke. Computational and Mathematical Methods in Medicine, **2016**(1), (2016).
12. Kosior, J.C., Buck, B., Wannamaker, R., Kate, M., Liapounova, N.A., Rempel, J.L. and Butcher, K.: Exploring reperfusion following endovascular thrombectomy: a proof of concept using perfusion angiography. Stroke, **50**(9), 2389-2395 (2019)
13. Su, R., van der Sluijs, P.M., Bobi, J., Taha, A., van Beusekom, H.M., van der Lugt, A., Niessen, W.J., Ruijters, D. and van Walsum, T.: Towards quantitative digital subtraction perfusion angiography: An animal study. Medical Physics, **50**(7), 4055-4066 (2023)
14. Nicolini, E., Iacobucci, M., De Michele, M., Ciacciarelli, A., Berto, I., Petraglia, L., Falcou, A., Cirelli, C., Biraschi, F., Lorenzano, S. and Linfante, I.: No-reflow phenomenon in acute ischemic stroke: an angiographic evaluation. Neurological Sciences, **44**(11), 3939-3948 (2023)
15. Frangi, A.F., Niessen, W.J., Vincken, K.L. and Viergever, M.A.: Multiscale vessel enhancement filtering. In Medical image computing and computer-assisted intervention—MICCAI 1998, Proceedings 1, 130-137. Springer Berlin Heidelberg (1998).